PTEP

Prog. Theor. Exp. Phys. **2019**, 053C02 (22 pages)
DOI: 10.1093/ptep/ptz030

A new approach for measuring the muon anomalous magnetic moment and electric dipole moment

M. Abe[1], S. Bae[2,3], G. Beer[4], G. Bunce[5], H. Choi[2,3], S. Choi[2,3], M. Chung[6], W. da Silva[7], S. Eidelman[8,9,10], M. Finger[11], Y. Fukao[1], T. Fukuyama[12], S. Haciomeroglu[13], K. Hasegawa[14], K. Hayasaka[15], N. Hayashizaki[16], H. Hisamatsu[1], T. Iijima[17], H. Iinuma[18], H. Ikeda[19], M. Ikeno[1], K. Inami[17], K. Ishida[20], T. Itahashi[21], M. Iwasaki[20], Y. Iwashita[22], Y. Iwata[23], R. Kadono[1], S. Kamal[24], T. Kamitani[1], S. Kanda[20], F. Kapusta[7], K. Kawagoe[25], N. Kawamura[1], B. Kim[2,3], Y. Kim[26], T. Kishishita[1], R. Kitamura[14], H. Ko[2,3], T. Kohriki[1], Y. Kondo[14], T. Kume[1], M. J. Lee[13], S. Lee[13], W. Lee[27], G. M. Marshall[28], Y. Matsuda[29], T. Mibe[1,30], Y. Miyake[1], T. Murakami[1], K. Nagamine[1], H. Nakayama[1], S. Nishimura[1], D. Nomura[1], T. Ogitsu[1], S. Ohsawa[1], K. Oide[1], Y. Oishi[1], S. Okada[20], A. Olin[4,28], Z. Omarov[26], M. Otani[1], G. Razuvaev[8,9], A. Rehman[30], N. Saito[1,31], N. F. Saito[20], K. Sasaki[1], O. Sasaki[1], N. Sato[1], Y. Sato[1], Y. K. Semertzidis[26], H. Sendai[1], Y. Shatunov[32], K. Shimomura[1], M. Shoji[1], B. Shwartz[9,32], P. Strasser[1], Y. Sue[17], T. Suehara[25], C. Sung[6], K. Suzuki[17], T. Takatomi[1], M. Tanaka[1], J. Tojo[25], Y. Tsutsumi[25], T. Uchida[1], K. Ueno[1], S. Wada[20], E. Won[27], H. Yamaguchi[1], T. Yamanaka[25], A. Yamamoto[1], T. Yamazaki[1], H. Yasuda[33], M. Yoshida[1], and T. Yoshioka[25,*]

[1]*High Energy Accelerator Research Organization (KEK), Ibaraki 319-1106, Japan*
[2]*Seoul National University, Seoul 08826, Republic of Korea*
[3]*Institute for Nuclear and Particle Astrophysics, Seoul 08826, Republic of Korea*
[4]*University of Victoria, British Columbia V8W 2Y2, Canada*
[5]*Retired*
[6]*Ulsan National Institute of Science and Technology (UNIST), Ulsan 44919, Republic of Korea*
[7]*LPNHE (CNRS/IN2P3/UPMC/UDD), Paris 75005, France*
[8]*Budker Institute of Nuclear Physics, Novosibirsk 630090, Russia*
[9]*Novosibirsk State University, Novosibirsk 630090, Russia*
[10]*Lebedev Physical Institute RAS, Moscow 119333, Russia*
[11]*Charles University, Prague 11000, Czech Republic*
[12]*Research Center for Nuclear Physics (RCNP), Osaka University, Osaka 567-0047, Japan*
[13]*Institute for Basic Science (IBS), Daejeon 34126, Republic of Korea*
[14]*Japan Atomic Energy Agency (JAEA), Ibaraki 319-1195, Japan*
[15]*Niigata University, Niigata 950-2181, Japan*
[16]*Tokyo Institute of Technology, Tokyo 152-8550, Japan*
[17]*Nagoya University, Aichi 464-8601, Japan*
[18]*Ibaraki University, Ibaraki 310-8502, Japan*
[19]*Japan Aerospace Exploration Agency (JAXA), Tokyo 229-8510, Japan*
[20]*RIKEN, Saitama 351-0198, Japan*
[21]*Graduate School / School of Science, Osaka University, Osaka 560-0043, Japan*
[22]*Institute for Chemical Research (ICR), Kyoto University, Kyoto 611-0011, Japan*
[23]*National Institute of Radiological Sciences (NIRS), Chiba 263-0024, Japan*
[24]*University of British Columbia, British Columbia V6T 1Z4, Canada*
[25]*Kyushu University, Fukuoka 819-0395, Japan*

[26]*Korea Advanced Institute of Science and Technology (KAIST), Daejeon 305-701, Republic of Korea*
[27]*Korea University, Seoul 02841, Republic of Korea*
[28]*TRIUMF, British Columbia V6T 2A3, Canada*
[29]*Graduate School of Arts and Sciences, The University of Tokyo, Tokyo 153-8902, Japan*
[30]*Graduate University for Advanced Studies (SOKENDAI), Ibaraki 305-0801, Japan*
[31]*J-PARC Center, Ibaraki 319-1106, Japan*
[32]*Budker Institute of Nuclear Physics SB RAS, Novosibirsk 630090, Russia*
[33]*Graduate School of Science, The University of Tokyo, Tokyo 113-0033, Japan*
*E-mail: yoshioka@phys.kyushu-u.ac.jp

Received January 9, 2019; Revised March 1, 2019; Accepted March 8, 2019; Published May 30, 2019

This paper introduces a new approach to measure the muon magnetic moment anomaly $a_\mu = (g-2)/2$ and the muon electric dipole moment (EDM) d_μ at the J-PARC muon facility. The goal of our experiment is to measure a_μ and d_μ using an independent method with a factor of 10 lower muon momentum, and a factor of 20 smaller diameter storage-ring solenoid compared with previous and ongoing muon $g-2$ experiments with unprecedented quality of the storage magnetic field. Additional significant differences from the present experimental method include a factor of 1000 smaller transverse emittance of the muon beam (reaccelerated thermal muon beam), its efficient vertical injection into the solenoid, and tracking each decay positron from muon decay to obtain its momentum vector. The precision goal for a_μ is a statistical uncertainty of 450 parts per billion (ppb), similar to the present experimental uncertainty, and a systematic uncertainty less than 70 ppb. The goal for EDM is a sensitivity of 1.5×10^{-21} $e \cdot$ cm.

Subject Index C07, C31

1. Introduction

The Standard Model (SM) [1,2] is an extremely successful theory of elementary particles. Even though more than 50 years have passed since it was first proposed, it remains the best effective theory that can describe physics below the weak scale. In fact, the recent discovery of the Higgs boson [3,4] and the measurements of its properties such as the signal strengths at the Large Hadron Collider (LHC) [5] have made our confidence in the SM stronger than ever.

Although the SM is such a successful theory, it is a firm expectation of many physicists that the SM is not the ultimate theory to describe physics at the shortest length scale. There are a number of reasons behind this. Firstly, there are as many as 19 free parameters in the SM whose values cannot be predicted from theory alone but can be determined only by experiments. Secondly, the SM must somehow be extended to accommodate gravity. It is known that this is difficult, and one may need a much larger framework such as string theory. Thirdly, in the SM, there is the gauge hierarchy problem, to explain why there are two vastly different fundamental scales, the weak scale $M_{\rm weak}$ ($= \mathcal{O}(100)$ GeV/c^2) and the Planck scale $M_{\rm Pl}$ ($= \mathcal{O}(10^{18})$ GeV/c^2).

Presently, many experiments are ongoing to search for new physics beyond the SM. Among the most promising are experiments at the LHC that directly probe physics at the TeV scale. To date, new physics has not been discovered, and a limit of $m_{\tilde{g},\tilde{q}} \gtrsim 1$ TeV/c^2 has been obtained on the masses of gluinos and squarks, for instance [5].

In view of this situation, the role played by precision measurements is becoming more crucial. Even when direct searches for new physics are limited in energy reach, indirect searches like precision measurements can become powerful probes of new physics. Moreover, it is reported [6–10] that there is at present a more than $3\,\sigma$ discrepancy between the experimental value of the muon's anomalous magnetic moment ($a_\mu = (g-2)/2$, where g is the Landé g-factor of the muon) [11] and the

prediction for it. In fact, the SM prediction quoted in Ref. [5] is

$$a_\mu(\mathrm{SM}) = (11\,659\,182.3 \pm 0.1 \pm 3.4 \pm 2.6) \times 10^{-10}\,, \tag{1}$$

where the uncertainties are from the electroweak, leading-order hadronic, and higher-order hadronic contributions, respectively. This value should be compared with the current experimental value [5,11],

$$a_\mu(\mathrm{exp}) = (11\,659\,209.1 \pm 5.4 \pm 3.3) \times 10^{-10}\,, \tag{2}$$

where the errors are the statistical and systematic uncertainties, respectively. The difference between Eqs. (1) and (2) is

$$\Delta a_\mu \equiv a_\mu(\mathrm{exp}) - a_\mu(\mathrm{SM}) = (26.8 \pm 7.6) \times 10^{-10}\,, \tag{3}$$

which means a $3.5\,\sigma$ deviation. This deviation may be the result of physics beyond the SM. This is a major motivation for new measurements of a_μ.

The reported deviation of the muon anomaly from the SM has another important implication. Since the contribution from new particles such as the smuon and the Kaluza–Klein excitations of the muon may be responsible for the deviation, it is natural to expect that effects from such new particles may also appear in closely related processes such as the muon electric dipole moment (EDM) [12], $\mu \to e\gamma$ and μ–e conversion in nuclei (see, e.g., Ref. [13] for a recent concise review). It is therefore valuable to study the muon EDM (d_μ), in addition to the muon $g-2$.

The current experimental result for a_μ is from the E821 experiment at Brookhaven National Laboratory (BNL) [11], which used the "magic gamma" approach with 100% polarized 3 GeV/c muons injected by an inflector magnet with 2–5% efficiency into a 14-meter-diameter storage ring built with 360 degree superconducting coils, 12 iron back-leg sectors and 36 iron pole sectors. With iron shims, a 1 part per million (ppm) field uniformity was achieved averaged over the muon orbit, with local non-uniformity of up to 100 ppm. Electrostatic focusing was used in the ring, and decay positrons (and electrons) were observed with calorimetry. A new measurement of a_μ is underway at Fermilab [14], using the BNL-E821 storage ring, with a new muon accumulator ring and significant magnetic shimming improvements, with expected gain in statistical and systematic uncertainties.

Our experiment introduced here is intended to measure a_μ and d_μ with a very different technique, using a 300 MeV/c reaccelerated thermal muon beam with 50% polarization, vertically injected into a magnetic resonance imaging (MRI)-type solenoid storage ring with 1 ppm local magnetic field uniformity for the muon storage region with an orbit diameter of 66 cm.

The vertical injection, invented for our experiment, will improve injection efficiency by more than an order of magnitude. Very weak magnetic focusing will be used in the ring. Silicon-strip detectors in the field will measure the momentum vector of the decay positrons.

Table 1 compares our experiment with the previous experiment BNL-E821, and the current experiment Fermilab-E989. The initial goal of our experiment is to reach the statistical uncertainty for a_μ of BNL-E821, with much smaller systematic uncertainties from sources different from the current method. The muon EDM goal is a statistical sensitivity of $1.5 \times 10^{-21}\ e\cdot\mathrm{cm}$ with a systematic uncertainty of $0.36 \times 10^{-21}\ e\cdot\mathrm{cm}$, which is a factor of 60 improvement over the present measurement [15], $d_\mu(\mathrm{exp}) = (0.0 \pm 0.2(\mathrm{stat.}) \pm 0.9(\mathrm{syst.})) \times 10^{-19}\ e\cdot\mathrm{cm}$.

Table 1. Comparison of BNL-E821, FNAL-E989, and our experiment.

	BNL-E821	Fermilab-E989	Our experiment
Muon momentum	3.09 GeV/c		300 MeV/c
Lorentz γ	29.3		3
Polarization	100%		50%
Storage field	$B = 1.45$ T		$B = 3.0$ T
Focusing field	Electric quadrupole		Very weak magnetic
Cyclotron period	149 ns		7.4 ns
Spin precession period	4.37 μs		2.11 μs
Number of detected e^+	5.0×10^9	1.6×10^{11}	5.7×10^{11}
Number of detected e^-	3.6×10^9	–	–
a_μ precision (stat.)	460 ppb	100 ppb	450 ppb
(syst.)	280 ppb	100 ppb	<70 ppb
EDM precision (stat.)	0.2×10^{-19} $e\cdot$cm	–	1.5×10^{-21} $e\cdot$cm
(syst.)	0.9×10^{-19} $e\cdot$cm	–	0.36×10^{-21} $e\cdot$cm

2. Overview of the experiment

The experiment measures a_μ and η. They are defined by the relations

$$a_\mu = \frac{g-2}{2} \quad \text{with} \quad \vec{\mu}_\mu = g\left(\frac{e}{2m}\right)\vec{s}, \quad \vec{d}_\mu = \eta\left(\frac{e}{2mc}\right)\vec{s}, \tag{4}$$

where e, m, and $\vec{s}$ are the electric charge, mass, and spin vector of the muon, respectively. Here, g is the Landé g-factor and η is a corresponding factor for the EDM. The experiment stores spin-polarized μ^+ in a magnet and the muons orbit in the uniform magnetic field. The spin of the muon precesses in the magnetic field. With the non-zero and positive value for $g-2$, the muon spin direction rotates faster than the momentum.

The spin precession vector with respect to its momentum in a static magnetic field $\vec{B}$ and electric field $\vec{E}$ is given as [16–21]

$$\vec{\omega} = \vec{\omega}_a + \vec{\omega}_\eta \tag{5}$$

$$= -\frac{e}{m}\left[a_\mu\vec{B} - \left(a_\mu - \frac{1}{\gamma^2-1}\right)\frac{\vec{\beta}\times\vec{E}}{c} + \frac{\eta}{2}\left(\vec{\beta}\times\vec{B} + \frac{\vec{E}}{c}\right)\right]. \tag{6}$$

Here $\vec{\omega}_a$ and $\vec{\omega}_\eta$ are precession vectors due to $g-2$ and EDM. $\vec{\beta}$ and γ are the velocity and Lorentz factor of the muon, respectively.

In the previous $g-2$ measurements, the energy of the muon was chosen to cancel the term of $\vec{\beta}\times\vec{E}$, which allowed for electrostatic focusing in the storage ring without affecting the muon spin precession to first order. A focusing field index of $n = 0.12$–0.14 was used, which was necessary to contain the muons captured from pion decay. In this proposed experiment, we greatly reduce the focusing requirement in the storage ring by using a reaccelerated thermal muon beam with a factor of 1000 smaller beam emittance. Very weak magnetic focusing with a field index of $n \sim 10^{-4}$ is enough to store the muon beam, using no electric field for focusing. Under this condition, Eq. (6) reduces to

$$\vec{\omega} = -\frac{e}{m}\left[a_\mu\vec{B} + \frac{\eta}{2}\left(\vec{\beta}\times\vec{B}\right)\right]. \tag{7}$$

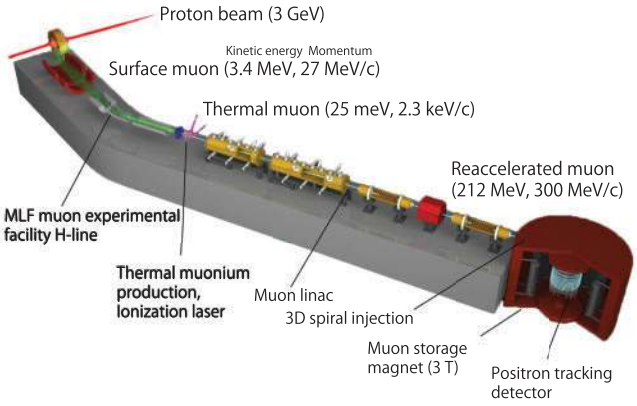

Fig. 1. Schematic view of the muon $g-2$/EDM experiment at J-PARC MLF.

There is no contribution from the $\vec{\beta}\times\vec{E}$ term at any beam energy. Since the precession vectors $\vec{\omega}_a$ and $\vec{\omega}_\eta$ are orthogonal, the $g-2$ and EDM precessions can be measured simultaneously with an appropriate detector design.

The key requirement for this new approach is a muon beam with low emittance. This can be realized with a source of positive muons with thermal energy followed by reacceleration, without increasing the transverse momentum spread. We note here that the stopping muons and their reacceleration steps will also allow us to frequently reverse the muon spins by using static electromagnetic fields. This feature will be a powerful tool to study rate-dependent systematics such as track reconstruction efficiency, and the effect of pile-up hits.

In the extraction of a_μ and η, the precession frequency $\vec{\omega}$ and the magnetic field $\vec{B}$ must be measured. The quantity $\vec{\omega}$ is measured by detecting positrons from muon decays during the storage. Like the other experiments that measure the muon anomalous moment, this method exploits the correlation of muon spin direction, or the polarization direction of the positive muon beam, with the energy and direction of the e^+ emitted in decay of the circulating stored muons [22]. By selecting the most energetic e^+, the rate of detection will show an oscillation in time due to the precession of the muon spin with respect to its momentum direction in the storage field. Detectors located radially inside the muon storage orbit will track the decay e^+. Our experiment records the number of higher-energy e^+ versus time in storage, as the muon spin precesses in the magnetic field.

The average magnetic field seen by the muons in the storage ring is measured by the Larmor precession frequency of a free proton (ω_p). This is obtained from a convolution of the magnetic field map and the muon beam distribution measured by the experiment.

Assuming that the EDM term is negligibly small compared with the $g-2$ term in Eq. (7), a_μ is obtained from $\omega_a = \frac{e}{m}a_\mu B$. By using ω_p, one can rewrite this equation to

$$a_\mu = \frac{R}{\lambda - R}, \tag{8}$$

where $R = \omega_a/\omega_p$ and $\lambda = \mu_\mu/\mu_p$ is the muon-to-proton magnetic moment ratio provided by separate experiments. The precision of the direct measurement of λ by muonium spectroscopy in the magnetic field is 120 ppb [23]. A new improved measurement of λ is being prepared at the J-PARC Materials and Life science experimental Facility (MLF) in the same beamline [24].

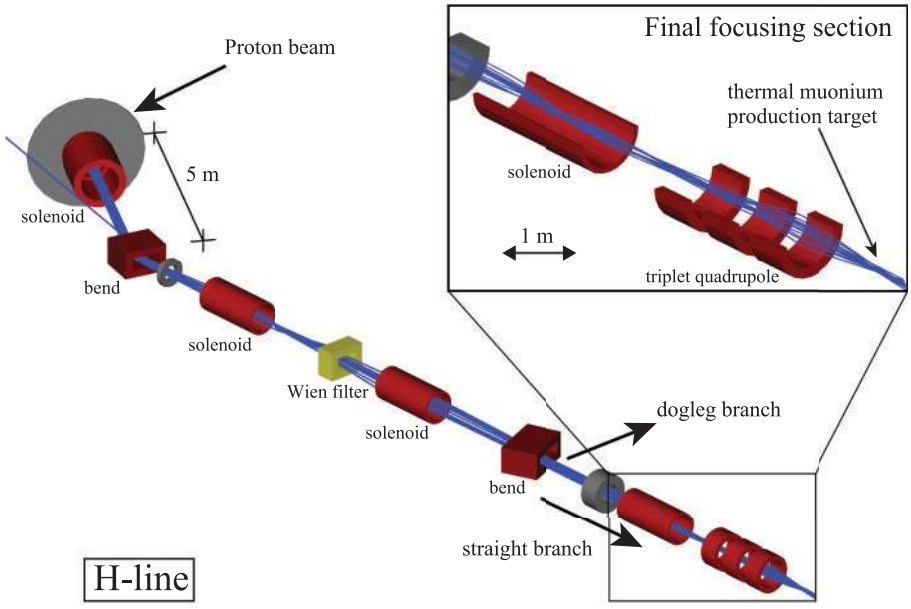

Fig. 2. Layout of the muon beamline (H-line) providing surface muons. Lines are simulated muon beam trajectories.

Our experiment will be installed at the muon facility (MUSE, Muon Science Establishment) [25] in the MLF of J-PARC. A schematic of the experimental setup is shown in Fig. 1. Experimental components and sensitivity estimations are described in the following sections.

3. Experimental facility and surface muon beam

A primary proton beam of 3 GeV kinetic energy with 1 MW beam power from the rapid cycle synchrotron hits a 2 cm thick graphite target to provide pulsed muon beams. The proton beam has a double-pulse structure, and each pulse is 100 ns in width (FWHM) with a 600 ns separation and 25 Hz repetition rate. Our experiment uses a surface muon beam. Surface muons are nearly 100% polarized positive muons from the decay of pions stopped at and near the target surface with the consequent momentum of 29.8 MeV/c and below. There are four beamlines extracting muon beams. Our experiment will use one of those, the H-line.

The H-line is a new beamline designed to deliver a high-intensity muon beam [26]. This is realized by adopting a large-aperture solenoid magnet to capture muons from the muon production target, wide gap bending magnets for momentum selection, and a pair of opposite directional solenoid magnets for efficient beam transport. The surface muon beam is focused onto a target to produce muonium atoms. The final focus condition is optimized to maximize the number of muons stopping in the muonium production target and to minimize the leakage magnetic field at the focal point. To fulfill these requirements, the final focusing includes a solenoid magnet followed by a triplet of quadrupole magnets. The layout of the H-line is shown in Fig. 2.

The intensity of the surface muon beam at the H-line is estimated to be $\sim 10^8$ per second at the designed proton beam power of 1 MW. The surface muon at the end of the beamline has a momentum centered at $p = 27$ MeV/c with momentum spread $\Delta p/p = 5\%$ (RMS). According to a beam transport simulation [27], the beam will be focused on the focal point with standard deviations of 31 and 14 mm in the horizontal and vertical directions, respectively.

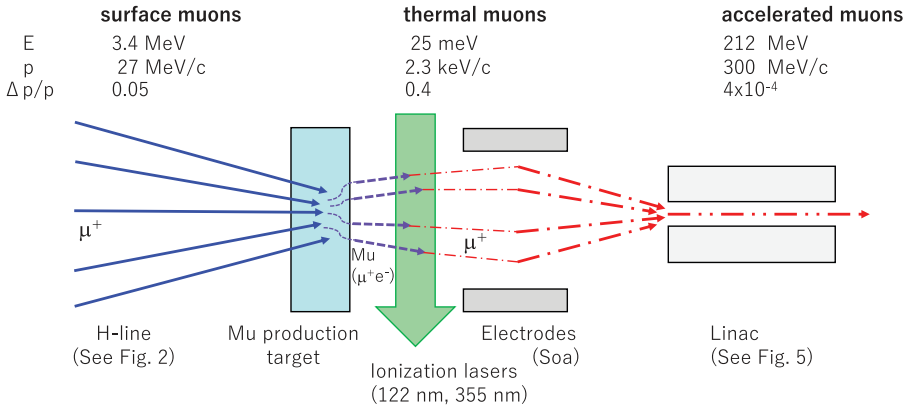

Fig. 3. Scheme of the reaccelerated thermal muon beam. The surface muon beam is thermalized in silica aerogel near the downstream edge of the Mu production target slab. Some of the muonium formed will diffuse to the surface of the slab and escape to vacuum with thermal energy. Intense laser beams strip the electron from muonium and the muon is accelerated by a static electric field followed by RF linac structures. Kinetic energy (E), total momentum (p), and its spread ($\Delta p/p$) at three stages are given.

4. Production of thermal muons from surface muons

The surface muon beam is converted at its final focus into a source of room-temperature muons. The first step is to slow down and thermalize the μ^+ in a carefully selected material, silica aerogel [28]. In this material, most of the muons form muonium atoms (μ^+e^-, or Mu) [29] that diffuse as neutral atoms into a vacuum region where Mu is ionized by laser excitation (Fig. 3). While the thermalization, conversion to Mu, diffusion, and ionization steps result in the loss of a significant fraction of the original surface muon beam, the characteristics of thermal muons after muonium ionization can be exploited as a source for acceleration and injection into a storage ring. A comparison of the kinematic characteristics of surface muons, a thermal source, and accelerated muons is summarized in Fig. 3.

Very low density silica aerogel is chosen as the muonium production target for high Mu formation probability (> 0.5) and low relaxation of the polarization. The maximum polarization is 50% after the statistical spin distribution among hyperfine states settles in the Mu atom. In addition, the silica aerogel provides a large mobility of Mu atoms within the aerogel structure such that they can be emitted with a near-thermal room-temperature energy distribution from the surface of the aerogel slab into the adjacent vacuum region.

The emission of Mu from aerogel, as well as the other important characteristics described above, has been discovered and verified by experiments on surface muon beamlines at TRIUMF [29,30] and J-PARC. The results showed that the emission probability was enhanced by an order of magnitude if the downstream aerogel surface was covered with a close-packed array of holes produced by laser ablation to a depth of the order of a few millimeters. The data are consistent with the assumption of Mu diffusion within the aerogel slab to the surface of the ablation holes followed by emission through the holes with speeds corresponding to thermal velocity near room temperature.

Figure 4 shows the simulated evolution of muonium into the laser irradiation region located at 1 mm from the surface of the aerogel slab. Here the simulation was performed using the diffusion model as explained above, where the diffusion parameter was predetermined so as to best describe the TRIUMF data [30]. The laser irradiation region is defined as a volume of $50 \times 200 \times 5$ mm^3 in the transverse directions and the longitudinal direction, respectively. This simulation indicates that the optimum time for the short ionization pulse is near 1.0 μs after the average time of arrival of the

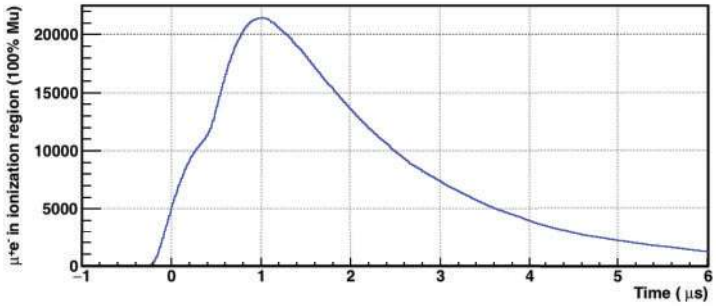

Fig. 4. Evolution of muonium into the laser irradiation region following diffusion and emission from a laser-ablated aerogel target. This is the result of a diffusion simulation with parameters that fit the results of Ref. [30]. The time origin is set at the middle of the double-pulse structure of the surface muons. The graph corresponds to the number of beam muons 3.23×10^6 and assumes 100% Mu formation per stopping muon. We expect the probability of Mu in the laser irradiation region to be 0.0034 ($= 0.52 \times 2.1 \times 10^4/(3.23 \times 10^6)$), where 0.52 is the initial formation probability of monism in the aerogel.

two surface muon pulses (0.6 μs apart). The efficiency for thermal muonium production is estimated to be 3.4×10^{-3} per surface muon.

A high-power ionizing laser system is synchronized to the periodic 25 Hz thermal Mu production at its maximum density in vacuum. The laser ionization consists of two processes. The first is $1s \rightarrow 2p$ excitation by a beam with a wavelength of 122 nm (Lyman-α), and the second is electron dissociation by a laser beam with a wavelength of 355 nm. The spectral linewidth and the pulse energy of the excitation beam is 80 GHz and 100 μJ, respectively. The pulse energy of the ionization beam is 440 mJ. The pulse width of each beam is 1 ns. The ionization efficiency was calculated to be 73% based on the transition rates given by theoretical excitation and dissociation cross sections multiplied with the expected laser photon density. The coherent Lyman-α light is generated by a nonlinear conversion in Kr gas from two pump laser beams. Two pump beams for the frequency conversion are generated by a distributed feedback laser followed by four stages of amplifiers and three stages of frequency converters with nonlinear optical crystals. Such an intense Lyman-α laser [31] is being developed in collaboration with the group developing an ultra-slow muon microscope, which is being used for the ionization of muonium at J-PARC U-line [32].

5. Acceleration

The room-temperature muons created by the laser ionization of thermal muonium will be accelerated to a momentum of 300 MeV/c (212 MeV in kinetic energy). The muons must be accelerated in a sufficiently short time compared with the muon lifetime of 2.2 μs to suppress muon decay loss during the acceleration. Another essential requirement for the acceleration is the suppression of transverse emittance growth. To satisfy these, a linac dedicated to this purpose will be used in our experiment. Figure 5 shows the schematic configuration of the muon linac. In accelerating the muons, the β increases rapidly with the kinetic energy. It is important to adopt adequate accelerating structures to obtain high acceleration efficiency, similar to proton linacs. The acceleration steps are 1) electrostatic acceleration with a Soa lens, 2) radio frequency quadrupole (RFQ), 3) interdigital H-type drift tube linac (IH-DTL), 4) disk-and-washer structure (DAW), and 5) disk-loaded traveling wave structure (DLS).

As the first acceleration step, thermal muons are accelerated from the ionization region by a pair of meshed metal plates and an electrostatic lens, a Soa lens [33]. Figure 6 shows distributions at the input of the RFQ linac simulated from distributions of the muon source [34]. The ellipses in the x–x'

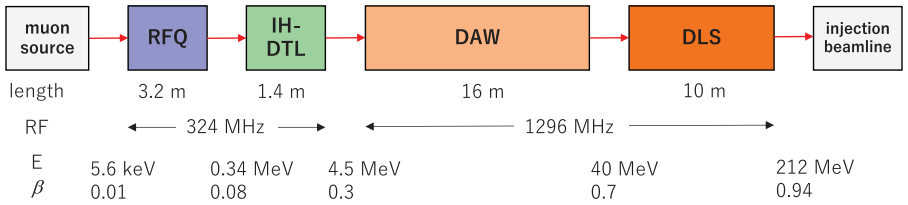

Fig. 5. Schematic configuration of the muon linac.

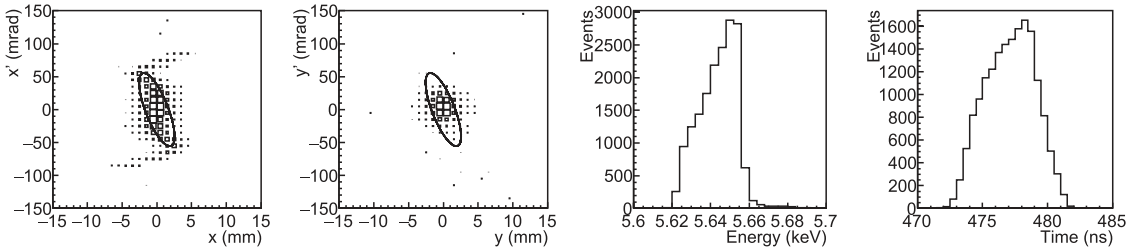

Fig. 6. Muon beam distribution at the RFQ entrance. The ellipses in the transverse distributions represent the matched ellipses of 1.0π mm mrad.

and y–y' distributions represent the matched ellipses of 1.0π mm mrad. The right panel represents the time structure at the entrance of the RFQ. Even though the pulse width of the dissociation laser is 1 ns, the time width at the RFQ entrance is 10 ns owing to the spatial distribution at ionization. Therefore, the beam from the source divides into three bunches during the acceleration in the RFQ at a frequency of 324 MHz. A spare RFQ of the J-PARC linac [35] will be used as a front-end structure accelerating the muons to 0.34 MeV [36]. A test of accelerating negative muonium ions is reported in Ref. [37].

The energy of the muon beam is boosted to 4.5 MeV with an IH-DTL. Unlike the Alvarez DTL, the IH-DTL uses the TE11 eigenmode, and π-mode acceleration [38]. With this mode, the acceleration length is halved compared with the 2π-mode acceleration. In addition, alternative phase focusing (APF) [39] is adopted. Since the use of APF eliminates the need for installing quadrupoles in the drift tubes, a higher shunt impedance per length can be achieved. The beam dynamics with such an IH-DTL was studied [40]. Sixteen cells are required to accelerate up to 4.5 MeV, and the total length of the cells is 1.29 m. The quality factor Q_0 is calculated to be 1.03×10^4, and the power dissipation is 320 kW. The effective shunt impedance per unit length is calculated to be 58 MΩ/m, which is competitive with those of other IH structures, taking our IH application to a relatively higher velocity region into account.

Following the IH-DTL, DAW structures with a frequency of 1296 MHz are used to accelerate to 40 MeV. The DAW is one of the coupled-cavity linacs that has large coupling between the cells and a high shunt impedance, especially in the middle β section [41]. The cell design was optimized for the velocities of $\beta = 0.3, 0.4, 0.5$, and 0.6 by using the SIMPLEX algorithm [42]. PARMILA [43] was used to design the beam dynamics of the DAW section. The acceleration gradient is determined to be 5.6 MV/m to keep the maximum electric field less than 0.9 times the Kilpatrick limit [44]. The field strengths of the quadrupole doublets between the modules and the number of cells in each module are determined with a condition that the phase advance in one focusing period is less than 90 degrees. The number of cells in a module is set to ten, and the phase advance is approximately 83 degrees in the first module, where the RF defocusing is strongest. The total length is 16.3 m with 15 modules. The estimated power dissipation is 4.5 MW.

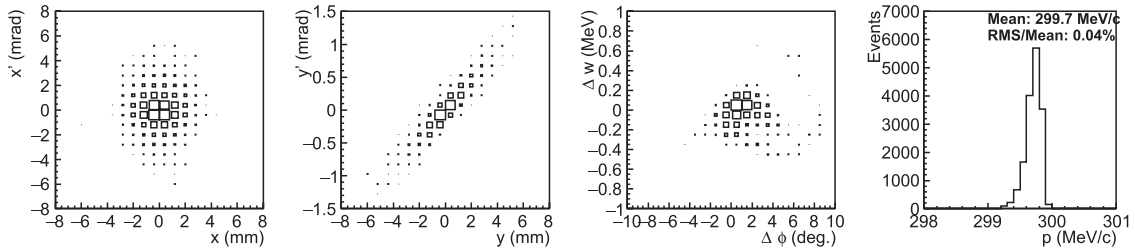

Fig. 7. Phase-space distributions at the muon linac exit. $\Delta\phi$ and Δw denote the phase and energy differences from the synchronized ones.

Table 2. Summary of the particle simulations through the muon linac.

	Soa	RFQ	IH	DAW	DLS
Transmission (%)	87	95	100	100	100
Decay loss (%)	17	19	1	4	1
$\varepsilon_{n,\mathrm{rms},x}$ (π mm mrad)	0.38	0.30	0.32	0.32	0.33
$\varepsilon_{n,\mathrm{rms},y}$ (π mm mrad)	0.11	0.17	0.20	0.21	0.21

Finally, the muons are accelerated from 40 MeV to 212 MeV by using a DLS, which is widely used for electron linacs. The advantage of the DLS is its high acceleration gradient, approximately 20 MV/m. An RF frequency of 1296 MHz is adequate for the wider phase space. The particular design feature of the DLS for muon acceleration, which is different from the general accelerating structure for an electron accelerator, is the variation of the disk spacing corresponding to the muon velocity [45]. The DLS section consists of four accelerating structures and the total length is approximately 10 m. Figure 7 shows the phase-space distributions at the exit of the DLS (muon linac exit) obtained by simulation. The estimated momentum spread is 0.04% (RMS).

The results of the acceleration simulations are summarized in Table 2. With this design of the muon linac, these simulations show that the transmission efficiency is kept high, and there is no significant growth of the beam emittance during the acceleration. The beam pulse width is 10 ns consisting of three microbunches, and the repetition rate is 25 Hz.

6. Beam injection and muon storage magnet

The muon beam must be injected into the muon storage magnet and the injection system must have minimum interference with the storage field. For reasons described later, a new method to inject the muon beam from the top of the magnet is adopted. After the linac, the muon beam follows a beam transport line to inject the muon beam at an incident pitch angle of -25 degrees. The beam transport line consists of two dipole magnets for bending the beam vertically, three normal quadrupole magnets to match the vertical momentum dispersion, and eight rotated quadrupole magnets to control the phase space to match the acceptance of injection into the magnet.

A 3 T MRI-type superconducting solenoid magnet will be used to complete the injection and store the muon beam. Figure 8 shows an overview of the muon storage magnet [46]. The muons are stored in a 3 T magnetic field with a cyclotron radius of 333 mm. This cyclotron radius is about a factor of 20 smaller than that for the BNL/Fermilab experiments. We take advantage of the advances in MRI magnet technology to fabricate such a small storage magnet with a highly uniform magnetic field in the muon storage region. As summarized in Table 3, the magnet system has four functions: (1)

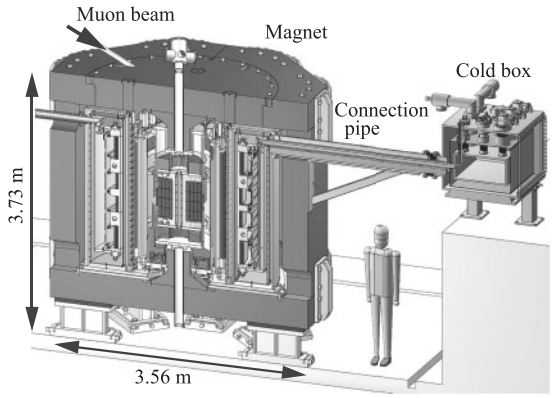

Fig. 8. Overview of the muon storage magnet.

Table 3. Functions and specifications of the magnet system.

Functions	Location	Specifications
Main field	$r = 333 \pm 15$ mm, $z = \pm 50$ mm	Axial field (B_{0z}) = 3 T Local uniformity < 1000 ppb Integrated uniformity along the orbit less than 100 ppb (peak-to-peak)
Injection field	$0.4 < z < 1.1$ m	Radial field with $B_r \times B_z > 0$
Kicker field	$\|z\| < 0.4$ m	Radial pulsed field created by two pairs of round-type kicker coils.
Storage field	$r = 333 \pm 15$ mm, $z = \pm 50$ mm	Weak magnetic focusing, n-index $\sim (1.5 \pm 0.5) \times 10^{-4}$

provide a highly uniform storage field, (2) provide the injection field, (3) provide the kicker field to store the muons, and (4) provide weak focusing for storage.

The main feature of the magnet is a highly homogeneous magnetic field of 3 T (main field) in the central region of the magnet, the storage region, where the muon beam is stored until its decay. The homogeneity of the magnetic field in the storage region is directly related to the sensitivity of the a_μ measurement. The integrated main magnetic field uniformity along the beam orbit in the storage region has to be carefully controlled with a precision of 100 ppb peak-to-peak. Figure 9 depicts the estimated relative field distribution in the r–z plane around the storage region averaged over the storage ring, where the z-axis is the center axis of the magnet along the direction of the magnetic field and r is the distance from the z-axis in a plane perpendicular to the axis. Averaged azimuthally over the muon orbit, the variation is estimated to be ± 50 ppb. The average field variation along the muon orbit for the BNL (E821) magnet was as large as ± 500 ppb [11].

The second function is to transport the muon beam from the outside of the storage magnet to the storage region. This transportation region is named the injection region. Due to the limited space of the storage magnet, the muon beam is not injected by the method used in the previous experiments of horizontal injection using an inflector magnet. Instead, a new 3D spiral injection scheme [48], as displayed in Fig. 10, is developed for this purpose.

A solenoid magnetic field shape is suitable for this new injection scheme. In the injection region, the radial component, B_r, of the magnetic field has to be carefully controlled from the top end of the magnet to the storage region for smooth injection. The left panel of Fig. 10 depicts the radial component of the fringe field along the beam in the injection volume. A 3D view of beam trajectories

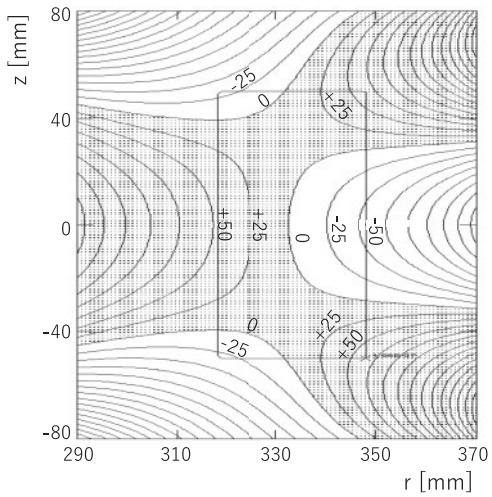

Fig. 9. Designed distribution of the main magnetic field relative to the reference field ($B_0 = 3$ T) averaged over the storage ring. In the dotted area, B is larger than B_0. Contour lines of residual magnetic field are at B_0, and $B_0\pm$ every 25 ppb (0.075 μT). The inset rectangle is the region of the stored muon orbit. The numbers in the figure are the residual magnetic field strengths in ppb. See more details in Ref. [47].

from the injection region to the storage region is also shown in the right panel. The muon beam is injected with a pitch angle of 440 mrad.

Open circles along the beam indicate points that correspond to the radial field values in the left panel. The beam momentum is deflected by B_r as it reaches the mid-plane of the solenoid magnet. Within the first three turns, the pitch angle becomes 40 mrad. We design the fringe field to control beam vertical motion. At the same time, this fringe field requires appropriate vertical–horizontal coupling (so-called X–Y coupling in the beam coordinate) to control vertical divergence, because of an axial symmetric shape in the fringe field. The X–Y coupling of the beam phase space, controlled by the magnets located just upstream of the solenoid, will be carefully tuned to minimize the vertical beam size in the storage region.

The third function of the magnet system is to provide a vertical kick, which will guide the beam inside the storage region. Two pairs of one-turn coils, the kicker coils positioned at heights of ± 0.4 m, generate a pulsed radial field $B_{\rm kick}$ to apply a vertical kick to the muon beam motion. Figure 11 shows the vertical beam motion from the start of the kick to the end, as well as the beam motion in the storage region.

The weak focusing field is the fourth function of the magnet system. In order to keep the beam inside the storage region within a stable orbit, a weak focusing magnetic field [47,48] will be used. The equations of the weak focusing magnetic field are

$$B_r = -n\frac{B_{0z}}{R}z, \tag{9}$$

$$B_z = B_{0z} - n\frac{B_{0z}}{R}(r - R) + n\frac{B_{0z}}{2R^2}z^2, \tag{10}$$

where B_{0z} (3 T) is the field strength in the z direction at the center of the storage region, R (333 mm) is the average radius of the stored beam, n is the field index.

The solenoid will be composed of five main coils wound with NbTi cable and the inner radius will be 0.8 m in the present design. An iron yoke is used to suppress magnetic flux leakage. The magnet

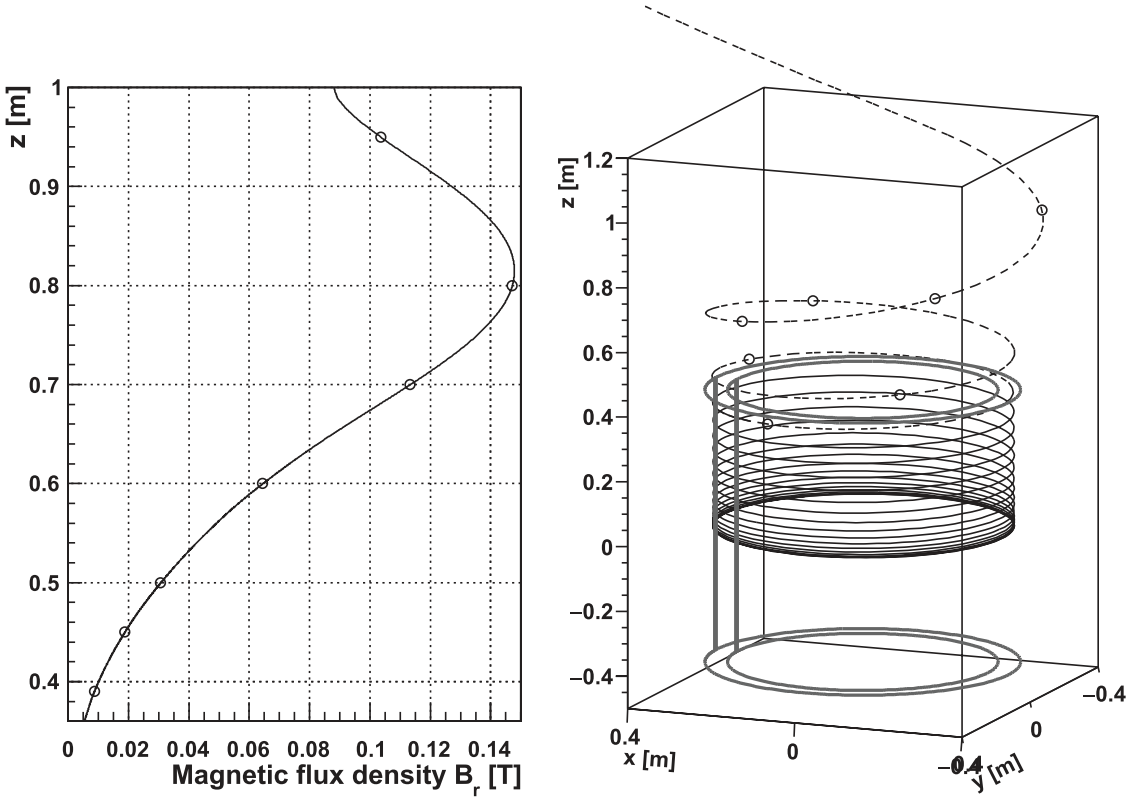

Fig. 10. Outline of the 3D injection scheme. The muon beam enters the solenoid obliquely from above into the injection region (the solenoid fringe field). Left: Radial component of the fringe field in the injection volume. Right: 3D view of the beam trajectories from the injection through the storage. The dotted line shows a design trajectory in the injection region. Open circles along the trajectory indicate the corresponding positions in the left plot. A solid line shows a design trajectory in the kicker region. Two pairs of one-turn coils for the kicker, which store the beam, are also shown.

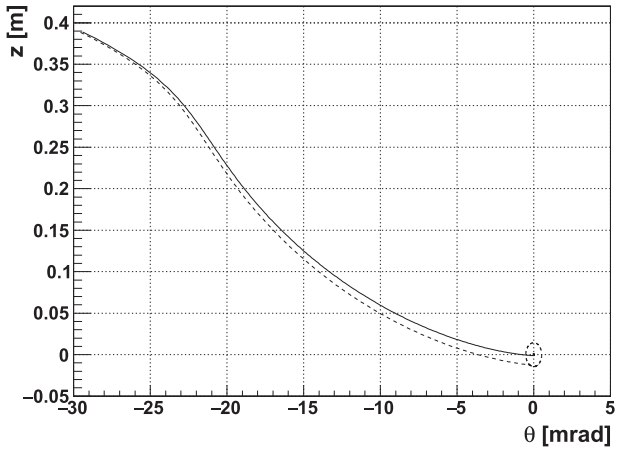

Fig. 11. Vertical beam motion during and after the kick for sample trajectories. The vertical axis is the vertical position and the horizontal axis is the pitch angle. The solid line is a design trajectory for the center of the beam. In the case that the muon does not stop on the mid-plane ($z = 0$ m) at the end of the kick, the muon will stay within the closed ellipse due to the weak focusing field, shown as a dotted line.

has pole tips at both ends of the solenoid coil to form the magnetic flux, with an entrance hole for injection.

The main coils will be operated in persistent current mode (PC mode) with a superconducting switch. The time constant of current decay during the nominal operation is generally expected to be less than 10 ppb/hour.

The weak focusing magnetic field is generated by dedicated coils, the weak focus coils, consisting of eight ring coils wound with NbTi cable that are aligned in the axial direction of the magnet. All ring coils are connected in series electrically and driven by a single power supply.

The magnetic field is shimmed by passive and active shimming systems. The former uses iron pieces, which are attached to support cylinders installed inside the magnet bore through holes in the iron poles in air. The magnetic field distribution is adjusted by changing the alignment pattern of the iron pieces. Active shimming is done using superconducting shim coils wound with NbTi cable. They are mainly used to compensate the error field changing with time in the storage region, and the residual error (expected to be small) after the magnetic field shimming by iron pieces. The shim coils consist of several saddle coils, which have a four-fold symmetry. Each coil is connected to an independent power supply to control each current.

The main coils, the weak focus coils, and the shim coils are immersed in liquid helium to ensure good temperature stability. The helium is recondensed by cryocoolers for long-term, stable, and cost-effective operation. Four cryocoolers and a heat exchanger for helium recondensation will be installed in a cold box, placed apart from the magnet cryostat. A connection pipe between the cold box and the magnet cryostat has a bellows connection, which is a soft connection in terms of mechanical structure, so that the vibration of cryocoolers will not be directly transferred to the magnet.

The magnetic field in the storage region is measured by a nuclear magnetic resonance (NMR) probe. A continuous-wave NMR (CW-NMR) magnetometer will be used in our experiment. The resonant absorption signal of protons ω_p in water samples is observed by using a fixed frequency source and a small sweeping magnetic field. The NMR probe will have a size of about 5–10 mm in diameter. Several NMR probes will be mounted on the three-axis moving stage in the radial, azimuthal, and vertical directions to scan the storage region for magnetic field mapping. The mapping probes are evacuated from the inside to outside of the storage region during the muon beam storage. The stages are driven by ultrasonic motors, which can work in the strong magnetic field. The ultrasonic motors have encoders so that the position of the NMR probe is controlled with a precision of below 0.1 mm.

In addition to the mapping probes, several other NMR probes will be installed below the storage region to measure time variation of the magnetic field strength, the fixed probes. The magnetic field strength will slightly and steadily decay in the PC mode, as described above, and it will also slightly fluctuate due to temperature variations. In order to compensate such small fluctuations of the magnetic field, and to know the best timing for the magnetic field restoration, we monitor the time variation of the magnetic field continuously at several appropriate field positions. The fixed probes do not monitor the deformation of the magnetic field distribution in the storage region but its time variations. A correlation between the magnetic field deformation and the field strength will be measured during the commissioning period for the detailed compensation of ω_p.

7. Positron detector

The positron detector is installed inside the storage magnet and measures positron tracks from decay of the stored muon beam. The muon storage region is kept in high vacuum not to cause beam emittance growth while the detector region is separated from the storage region by a polyimide film

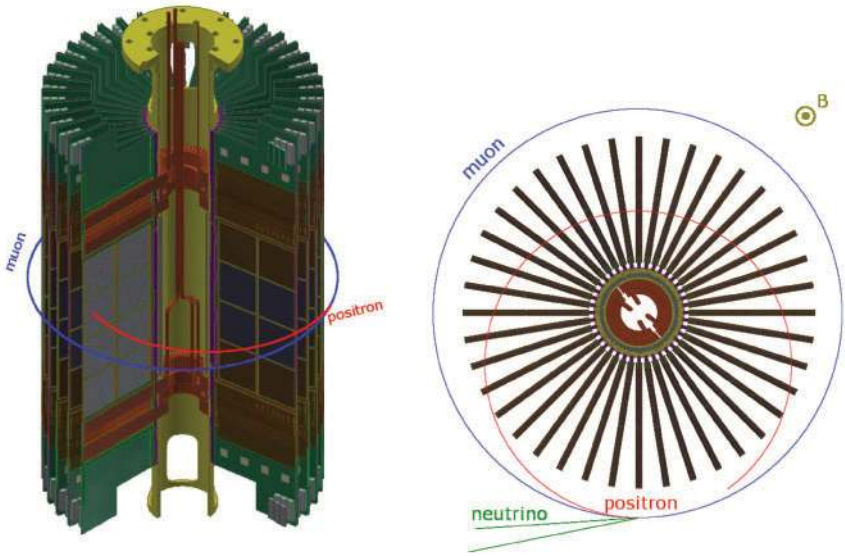

Fig. 12. Perspective view (left) and top view (right) of the positron detector.

and is kept in medium vacuum. A muon with a momentum of 300 MeV/c circulates with a radius of 333 mm and decays to a positron, a neutrino, and an antineutrino with a dilated lifetime of 6.6 μs. The cyclotron period is 7.4 ns. Since the anomalous precession period is 2.1 μs, muons circulate the ring about 300 times on average during one revolution of muon spin. The goals of the detector are to measure ω_a and the up–down asymmetry of positron direction due to EDM.

Due to non-conservation of parity in the weak decay of muons, the average positron energy is higher when positrons are emitted closer to the muon spin [49]. By measuring high-energy positrons selectively, positrons emitted forward can be selected and the time variation of muon spin with respect to the muon momentum direction can be measured. The sensitivity becomes maximum when positrons with momenta above 200 MeV/c are counted. The maximum momentum of decay positrons is 309 MeV/c while momenta in the range from 200 MeV/c to 275 MeV/c will be used for the analysis.

Positrons emitted within the 3 T magnetic field move in a spiral orbit. This trajectory is detected by radially arranged silicon-strip sensors. Geometrical coverage of the detector is 90–290 mm in the radial direction and within $\pm$200 mm in height. The layout of the detector is shown in Fig. 12.

The muon beam time structure following acceleration to 300 MeV/c is a pulse of 10 ns width consisting of three microbunches, with a repetition rate of 25 Hz. This is the time structure of the fill of the muon storage ring. The number of muons per fill is about 10^4. The measurement will be performed in an interval following a fill of 33 μs, which is five times longer than the time-dilated muon lifetime. The rate of positrons changes by a factor of 160 from the beginning to the end of the measurement. Thus, the detector is required to be stable against the change of positron rate; otherwise, the measured ω_a would be biased.

The detector consists of 40 radial modules called vanes. Each vane consists of 16 sensors, half of which measure the radial coordinate and half the axial coordinate of ionization. Sensors are made by single-sided p-on-n silicon technology [50]. The active area of a sensor is 97.28 mm $\times$ 97.28 mm with a thickness of 0.32 mm. A sensor has two blocks of 512 strips with a pitch of 190 μm. Therefore a vane has 16 384 strips, with 655k total strips for the detector.

The data from the silicon-strip sensors are read out by front-end boards with an application-specific integrated circuit (ASIC) on the detector with a 5 ns time stamp, followed by readout boards with the Versa Module Eurocard (VME) interface, then collected by the PC farm through a gigabit ethernet switch. The data acquisition system is based on DAQ-Middleware [51]. The estimated rate of data from the whole detector is 360 MB/s (or 14.4 MB/fill).

One readout ASIC has 128 channels for analog and digital blocks. The dynamic range of input charge is required to be greater than four minimum ionizing particles (MIP) equivalent with linearity. Equivalent noise charge is required to be less than 1600 e^- with an input capacitance of 30 pF, which corresponds to a signal-to-noise ratio greater than 15 for a 1 MIP signal. One of the major systematic uncertainties on ω_a is the hit-timing shift due to pile-up hits. If several charged particles pass through the same sensor strip within the pulse width, the signal pulse shape is distorted and the detected timing shifts. Since the pile-up rate changes as a function of time, this timing shift causes a systematic shift in the ω_a measurement. To constrain this effect, the peaking time at 1 MIP charge is required to be less than 50 ns and the time-walk between 0.5 MIP and 3 MIP is required to be less than 5 ns.

The system clock is provided by the Global Positioning System (GPS)-synchronized Rb frequency standard [52], and it is distributed with real-time control signals to the readout boards and the front-end board through the timing control/monitor board. Long-term stability of the system clock frequency is confirmed better than 10^{-11}.

The stringent requirement on detector alignment comes from the EDM measurement [53]. Alignment accuracies of vanes with respect to the magnetic field direction are required to be better than 10 μrad for skew, i.e., the angle around an axis normal to the vane. In order to ensure the required accuracies, alignment changes for the vanes are detected and monitored during operation using an absolute distance interferometer system [54].

At the beginning of the interval after the fill, about 30 positrons are produced from muon decay in 5 ns, which is one time window of the data taking. The maximum hit rate per silicon sensor strip is 7×10^{-3} per time stamp. To find positron tracks in such a condition, a positron track candidate is identified from hits in the detector using the property that high-momentum positron tracks leave nearly straight lines in the ϕ–z plane, where ϕ is the angle around the z-axis. Figure 13 shows event displays and reconstructed tracks obtained from simulation. In the ϕ–z plane (bottom right), straight lines used as seeds for track finding are shown. A Hough transformation [55,56] is used to find straight lines in the plane and hits on a straight line are used as the seed. A track momentum is obtained by track fitting with a Kalman filter [57]. With this algorithm, a track reconstruction efficiency greater than 90% is achieved in the positron energy range of 200 MeV $< E <$ 275 MeV even at the highest positron rate.

The muon decay position is determined by the closest point of approach between the reconstructed positron trajectory and the muon beam orbit. The muon decay time at the decay position is measured by extrapolating the time of hits in reconstructed positron tracks. One way to estimate decay time is to use the average time of reconstructed track hits. Another approach is to use the transition timing of hits with the 5 ns time stamp when detector hits are distributed with a width larger than one time stamp. The latter method has better timing resolution than the former but it is applicable only when the transition occurs within a track. The two definitions of decay time can be cross-checked with each other.

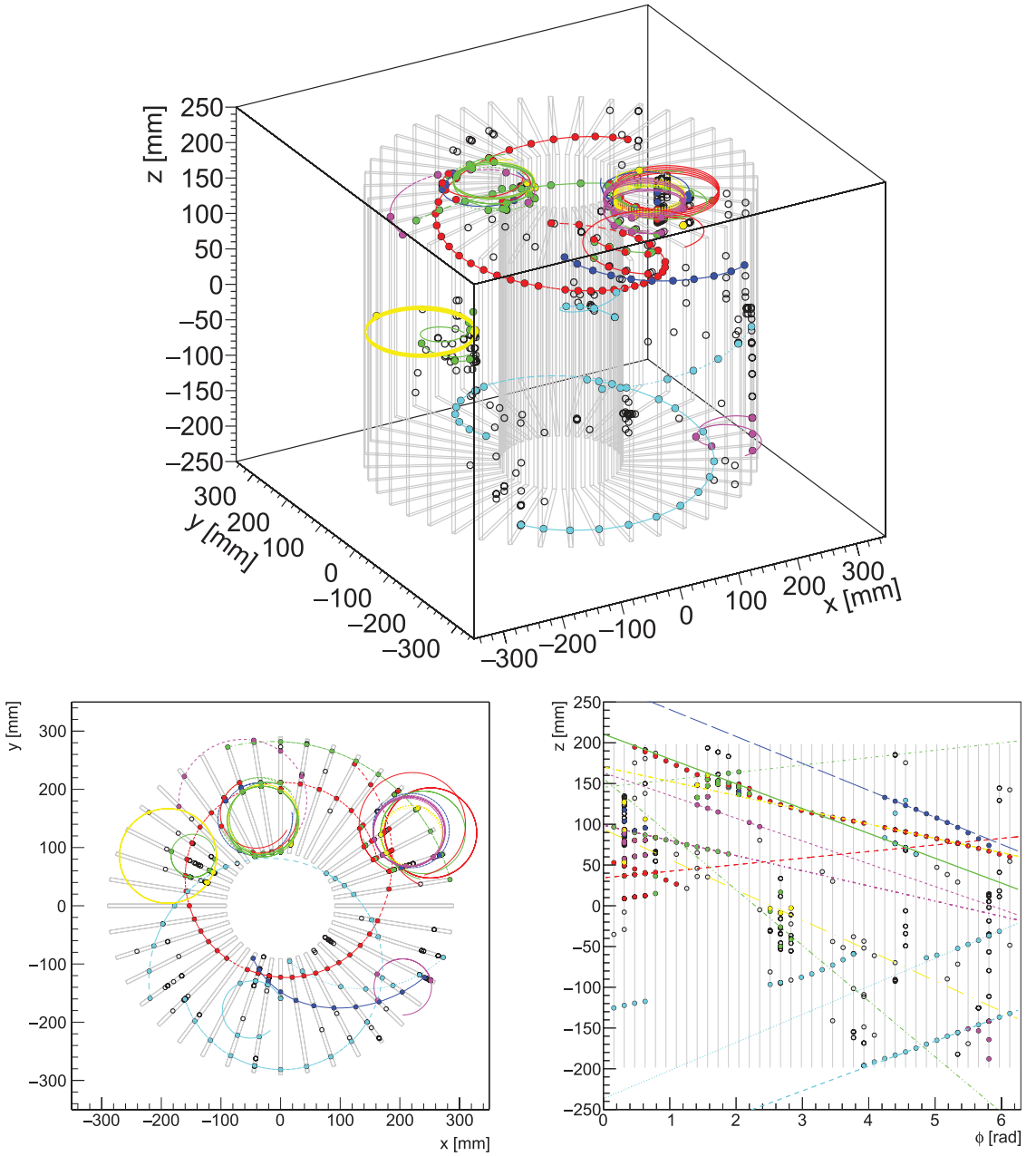

Fig. 13. All reconstructed hits from 25 muon decays obtained from simulation projected onto the horizontal (x–y) plane (bottom left) and in the ϕ–z plane (bottom right), and perspective view in 3D space (top) are shown. There are two positron tracks in the energy range of 200 MeV $< E <$ 275 MeV. Track candidate hits are shown by colored dots and the other hits are shown by white dots. Reconstructed track orbits are shown by colored curves (top and bottom left) and straight lines for track finding are shown (bottom right).

8. Estimation of the number of reconstructed positrons

Efficiencies of steps from the surface muon production to the detection of positrons are studied by a chain of simulations. Table 4 shows the breakdown of the efficiencies. The simulations include surface muon production, thermal muon production, reacceleration, injection to the muon storage magnet, muon beam dynamics in storage, and finally the detection of the positron. The simulation of surface muon production [34] and thermal muon production is optimized by the experimental

Table 4. Breakdown of estimated efficiency.

Subsystem	Efficiency	Subsystem	Efficiency
H-line acceptance and transmission	0.16	DAW decay	0.96
Mu emission	0.0034	DLS transmission	1.00
Laser ionization	0.73	DLS decay	0.99
Metal mesh	0.78	Injection transmission	0.85
Initial acceleration transmission and decay	0.72	Injection decay	0.99
RFQ transmission	0.95	Kicker decay	0.93
RFQ decay	0.81	e^+ energy window	0.12
IH transmission	0.99	Detector acceptance of e^+	1.00
IH decay	0.99	Reconstruction efficiency	0.90
DAW transmission	1.00		

data on surface muon yield at the existing beamline and measurements of the muonium space-time distribution [30], respectively. The total efficiency is 1.3×10^{-5} per initial muon at production. At a proton beam power of 1 MW, the expected number of positrons is 5.7×10^{11} for 2.2×10^7 seconds of data taking.

9. Extraction of a_μ and EDM

The values of ω_a and η are obtained from the muon decay time distribution. The muon decay time is reconstructed from the positron track as described in Sect. 7. A simulated time spectrum for detected positrons in the energy range between 200 MeV and 275 MeV is shown in Fig. 14 (left). The anomalous precession frequency ω_a is extracted by fitting to the data. Alternatively, one can make a ratio of data taken with opposite initial spin orientations. This will be useful to study early-to-late changes in the detector performance.

The value of ω_p, from which we determine the average magnetic field seen by the muons in the storage ring, is measured by independent measurements of the magnetic field map in the storage ring provided from the proton NMR data and the muon beam distribution deduced from tracing back the positron track to the muon beam. A blind analysis will be done as was done in the previous BNL experiment, separating the results for magnetic field and spin precession until all systematic uncertainties are finalized.

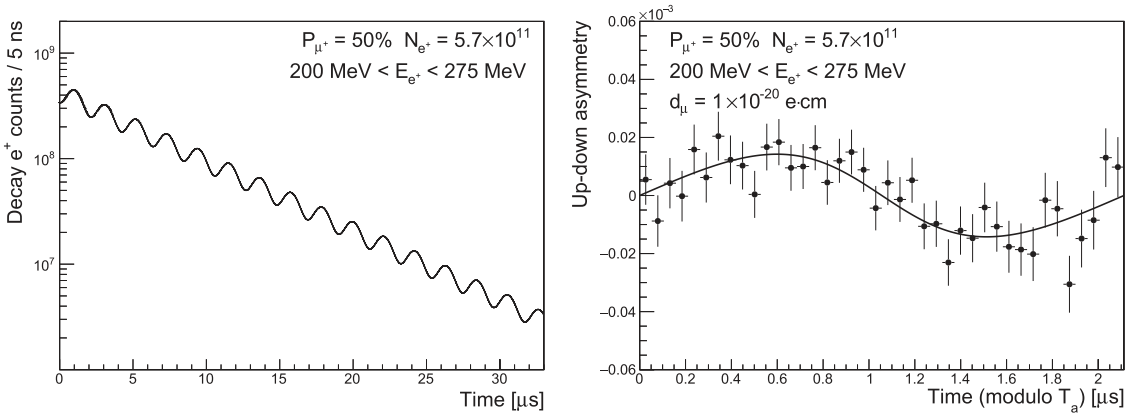

Fig. 14. Simulated time distribution of reconstructed positrons (left) and the up–down asymmetry as a function of time modulo of the $g-2$ period (right). The solid curve is the fit to simulated data.

Table 5. Summary of statistics and uncertainties.

	Estimation
Total number of muons in the storage magnet	5.2×10^{12}
Total number of reconstructed e^+ in the energy window [200, 275 MeV]	5.7×10^{11}
Effective analyzing power	0.42
Statistical uncertainty on ω_a [ppb]	450
Uncertainties on a_μ [ppb]	450 (stat.)
	< 70 (syst.)
Uncertainties on EDM [10^{-21} e·cm]	1.5 (stat.)
	0.36 (syst.)

Table 6. Estimated systmatic uncertainties on a_μ.

Anomalous spin precession (ω_a)		Magnetic field (ω_p)	
Source	Estimation (ppb)	Source	Estimation (ppb)
Timing shift	< 36	Absolute calibration	25
Pitch effect	13	Calibration of mapping probe	20
Electric field	10	Position of mapping probe	45
Delayed positrons	0.8	Field decay	< 10
Diffential decay	1.5	Eddy current from kicker	0.1
Quadratic sum	< 40	Quadratic sum	56

After the ω_a and ω_p are extracted from the experimental data, a_μ is obtained from Eq. (8). Table 5 summarizes statistics and uncertainties for 2.2×10^7 seconds of data taking. The estimated statistical uncertainty on ω_a is 450 ppb, while the statistical uncertainty on ω_p will be negligibly small. Thus, the statistical uncertainty of a_μ would be 450 ppb.

Systematic uncertainties on ω_a are estimated as follows. A timing shift due to pile-up of hits in the tracking detector is estimated as less than 36 ppb in the detector simulation by taking into account time responses of readout electronics. A correction for a pitch angle is not necessary in the case of muon storage in a perfect weak magnetic focusing field [58]. A difference in the actual field distribution from the perfect case leads to a systematic uncertainty of 13 ppb, which is estimated from a precision spin-tracking simulation of muon beam storage. Residual electric fields modify ω_a through the $\vec{\beta} \times \vec{E}$ term. With 1 mV/cm monitoring resolution for an E-field, the error on ω_a is 10 ppb. Other effects, such as distortion of the time distribution due to high-energy positrons hitting the detector at delayed timing and differential decay due to the momentum spread of the muon beam, are of the order of 1 ppb. In the ω_p measurement, absolute calibration of the standard probe has an uncertainty of 25 ppb. The positioning resolution of the field mapping probe at the calibration point and the muon storage region leads to 20 ppb and 45 ppb uncertainties, respectively. Other effects, such as field decay and eddy currents from the kicker, are less than 10 ppb. Table 6 summarizes systematic uncertainties on a_μ. We estimate that the combined systematic uncertainty on a_μ is less than 70 ppb.

A muon EDM will produce muon spin precession out of the horizontal plane that is defined by the ideal muon orbit. This can be seen from Eq. (7) where the second term is the EDM term, which is perpendicular to the a_μ term. Due to the fact that the EDM term generates vertical motion of the spin, one can extract the EDM term from the oscillation of the up and down asymmetry $\mathcal{A}_{\mathrm{UD}}(t)$ in

the number of positrons detected,

$$\mathcal{A}_{\rm UD}(t) = \frac{N^{\rm up}(t) - N^{\rm down}(t)}{N^{\rm up}(t) + N^{\rm down}(t)} = \frac{PA_{\rm EDM}\sin(\omega t + \phi)}{1 + PA\cos(\omega t + \phi)}, \tag{11}$$

where P, A, and ϕ are the polarization of the muon and the effective analyzing power of muon decay, and the phase of muon spin with respect to thhe direction of the momentum, respectively. $A_{\rm EDM}$ is the effective analyzing power associated with the EDM. A simulated up–down asymmetry in the case of $d_\mu = 1 \times 10^{-20}\ e \cdot$ cm is shown in Fig. 14 (right). The estimated statistical sensitivity for EDM is $1.5 \times 10^{-21}\ e \cdot$ cm (see Table 5).

A major source of systematic uncertainty on EDM is detector misalignment with respect to the plane of the muon storage. The alignment resolution is estimated as 3.6 μrad [59] from the resolution of the alignment monitor system made with optical frequency comb technology. This leads to a systematic uncertainty of $0.36 \times 10^{-21}\ e \cdot$ cm. The effects of axial electric field and radial magnetic field [60] are both less than $10^{-24}\ e \cdot$ cm, thus negligibly small.

10. Summary

A new method of measuring a_μ and EDM of the muon is described. Our experiment utilizes a low-emittance muon beam prepared by reaccelerating thermal-energy muons created from laser-resonant ionization of muonium atoms. The low-emittance muon beam allows use of very weak magnetic focusing and the selected low muon momentum (300 MeV/c) leads to the use of a compact magnetic storage ring, instead of the strong electric focusing at the magic momentum (3 GeV/c) used by the previous and ongoing $g-2$ experiments. A novel 3D spiral injection method with a pulsed magnetic kick is adopted to store the muon beam in the storage ring efficiently. Our experiment reconstructs positron tracks from muons decaying during their storage with a tracking detector consisting of silicon-strip sensors.

Our experiment intends to reach statistical uncertainties for a_μ of 450 ppb and for muon EDM of $1.5 \times 10^{-21}\ e \cdot$cm, for an acquisition time of 2.2×10^7 seconds. The statistical precision is comparable to that of the BNL experiment. The EDM sensitivity is about two orders of magnitude higher than the BNL limit. Present estimates of systematic uncertainties on a_μ and EDM are factors of seven and four smaller than the statistical uncertainties, respectively. Our experiment with statistically limited sensitivity will test the $3\,\sigma$ deviation on $g-2$ reported by the BNL experiment with significantly different and improved systematic uncertainties and will search for new sources of T-violation in the muon EDM with unprecedented sensitivity.

Acknowledgements

The authors would like to thank the KEK and the J-PARC muon section staff for their strong support. This work is supported by Japan Society for the Promotion of Science (JSPS) KAKENHI Grant Nos. JP19740158, JP23108001, JP23740216, JP25800164, JP26287053, JP26287055, JP15H03666, JP15H05742, JP16H03987, JP16J07784, JP16K13810, JP16K05323, JP17H01133, JP17H02904, JP17K05466, JP17K18784, JP18H01239, and JP18H03707. This work is also supported by the Korean National Research Foundation Grant Nos. NRF- 2015H1A2A1030275, NRF-2015K2A2A4000092, and NRF-2017R1A2B3007018; the Russian Foundation for Basic Research Grant No. RFBR 17-52-50064, which is part of the Japan–Russia Research Cooperative Program; the Russian Science Foundation Grant No. 17-12-01036; the Russian Ministry of Science and Higher Education Agreement 14.W03.31.0026; the US–Japan Science and Technology Cooperation Program in High Energy Physics; the Discovery Grants Program of the Natural Sciences and Engineering Research Council of Canada; and the Institute for Basic Science (IBS) of Republic of Korea under Project No. IBS-R017-D1-2018-a00.

References

[1] S. Weinberg, Phys. Rev. Lett. **19**, 1264 (1967).
[2] A. Salam, Conf. Proc. C **680519**, 367 (1968).
[3] G. Aad et al. [ATLAS Collaboration], Phys. Lett. B **716**, 1 (2012).
[4] S. Chatrchyan et al. [CMS Collaboration], Phys. Lett. B **716**, 30 (2012).
[5] M. Tanabashi et al. [Particle Data Group], Phys. Rev. D **98**, 030001 (2018).
[6] A. Keshavarzi, D. Nomura, and T. Teubner, Phys. Rev. D **97**, 114025 (2018).
[7] M. Davier, A. Hoecker, B. Malaescu, and Z. Zhang, Eur. Phys. J. C **77**, 827 (2017).
[8] F. Jegerlehner, *The Anomalous Magnetic Moment of the Muon* (Springer, Berlin, 2017), Springer Tracts in Modern Physics Vol. 274, p. 1.
[9] M. Benayoun, P. David, L. DelBuono, and F. Jegerlehner, Eur. Phys. J. C **75**, 613 (2015).
[10] T. Blum, P. A. Boyle, V. Gülpers, T. Izubuchi, L. Jin, C. Jung, A. Jüttner, C. Lehner, A. Portelli, and J. T. Tsang [RBC and UKQCD Collaborations], Phys. Rev. Lett. **121**, 022003 (2018).
[11] G. W. Bennett et al. [Muon $g-2$ Collaboration], Phys. Rev. D **73**, 072003 (2006).
[12] A. Crivellin, M. Hoferichter, and P. Schmidt-Wellenburg, Phys. Rev. D **98**, 113002 (2018).
[13] P. Paradisi, EPJ Web Conf. **118**, 01026 (2016).
[14] J. Grange et al. [Muon $g-2$ Collaboration], arXiv:1501.06858 [physics.ins-det] [Search INSPIRE].
[15] G. W. Bennett et al. [Muon $g-2$ Collaboration], Phys. Rev. D **80**, 052008 (2009).
[16] L. H. Thomas, Philos. Mag. **3**, 1 (1927).
[17] V. Bargmann, L. Michel, and V. L. Telegdi, Phys. Rev. Lett. **2**, 435 (1959).
[18] D. F. Nelson, A. A. Schupp, R. W. Pidd, and H. R. Crane, Phys. Rev. Lett. **2**, 492 (1959).
[19] I. B. Khriplovich, Phys. Lett. B **444**, 98 (1998).
[20] T. Fukuyama and A. J. Silenko, Int. J. Mod. Phys. A **28**, 1350147 (2013).
[21] T. Fukuyama, Phys. Lett. B **786**, 45 (2018).
[22] E. J. Konopinski, Annu. Rev. Nucl. Sci. **9**, 99 (1959).
[23] W. Liu et al., Phys. Rev. Lett. **82**, 711 (1999).
[24] K. Shimomura, Hyperfine Interact. **233**, 89 (2015).
[25] W. Higemoto, R. Kadono, N. Kawamura, A. Koda, K. M. Kojima, S. Makimura, S. Matoba, Y. Miyake, K. Shimomura, and P. Strasser, Quantum Beam Sci. **1**, 11 (2017).
[26] N. Kawamura et al., Prog. Theor. Exp. Phys. **2018**, 113G01 (2018).
[27] T. J. Roberts et al., Proc. PAC07 (2007) 3468; G4beamline (available at: http://g4beamline.muonsinc.com, date last accessed April 24, 2019).
[28] M. Tabata, I. Adachi, H. Kawai, T. Sumiyoshi, and H. Yokogawa, Nucl. Instrum. Meth. A **668**, 64 (2012).
[29] P. Bakule et al., Prog. Theor. Exp. Phys. **2013**, 103C01 (2013).
[30] G. A. Beer et al., Prog. Theor. Exp. Phys. **2014**, 091C01 (2014).
[31] N. Saito, Y. Oishi, K. Miyazaki, K. Okamura, J. Nakamura, O. A. Louchev, M. Iwasaki, and S. Wada, Opt. Express **24**, 7566 (2016).
[32] A. Pant et al., JPS Conf. Proc. **21**, 011060 (2018).
[33] K. F. Canter, P. H. Lippel, W. S. Crane, and A. P. Mills Jr, Modified Soa immersion lens positron gun, in *Positron Studies of Solids, Surfaces and Atoms* (World Scientific, Singapore, 1986), p. 199.
[34] M. Otani, N. Kawamura, T. Mibe, T. Yamazaki, K. Ishida, and G. Marshall, Proc. IPAC2018, TUPAK007 (2018).
[35] Y. Kondo et al., Phys. Rev. ST Accel. Beams **16**, 040102 (2013).
[36] Y. Kondo, K. Hasegawa, M. Otani, T. Mibe, N. Saito, and R. Kitamura, Proc. IPAC2015, p. 3801 (2015).
[37] S. Bae et al., Phys. Rev. Accel. Beams **21**, 050101 (2018).
[38] J. P. Blewett, Proc. Symp. CERN sur les Accelerateurs de Haute Energie et la Physique des Mesons π v.1, p. 162 (1956).
[39] M. L. Good, Phys. Rev. **92**, 538 (1953).
[40] M. Otani, T. Mibe, M. Yoshida, K. Hasegawa, Y. Kondo, N. Hayashizaki, Y. Iwashita, Y. Iwata, R. Kitamura, and N. Saito, Phys. Rev. Accel. Beams **19**, 040101 (2016).
[41] V. G. Andreev, V. M. Belugin, V. G. Kulman, E. A. Mirochnik, and B. M. Pirozhenko, Proc. 1972 Proton Linear Accelerator Conference, p. 114 (1972).
[42] M. Otani et al., Proc. IPAC2016, p. 1543 (2016).
[43] H. Takeda, Parmila, Technical report, LA-UR-98-4478. December 16, 2005.

[44] W. D. Kilpatrick, Rev. Sci. Instrum. **28**, 824 (1957).
[45] Y. Kondo, K. Hasegawa, M. Otani, T. Mibe, M. Yoshida, and R Kitamura, J. Phys.: Conf. Ser. **874**, 012054 (2017).
[46] K. Sasaki et al., IEEE Trans. Appl. Supercond. **26**, 0605604 (2016).
[47] M. Abe, Y. Murata, H. Iinuma, T. Ogitsu, N. Saito, K. Sasaki, T. Mibe, and H. Nakayama, Nucl. Instrum. Meth. A **890**, 51 (2018).
[48] H. Iinuma, H. Nakayama, K. Oide, K.-i. Sasaki, N. Saito, T. Mibe, and M. Abe, Nucl. Instrum. Meth. A **832**, 51 (2016).
[49] L. Michel, Proc. Phys. Soc. A **63**, 514 (1950).
[50] Hamamatsu Photonics K.K. (available at: https://www.hamamatsu.com/jp/en/product/type/S13804/index.html, date last accessed April 24, 2019).
[51] Y. Yoshiji et al., Proc. IEEE/NPSS Real Time Conf., p. 1 (2017).
[52] FT-001S, Freqtime Co. Ltd. (available at: http://freqtime.co.jp/product/ft-001s, date last accessed April 24, 2019).
[53] S. Nishimura et al., JPS Conf. Proc. **8**, 025015 (2015).
[54] T. Kume et al., "Precise alignment monitor by using optical frequency comb for the muon g-2/EDM experiment at J-PARC", poster presented at 14th International Conference on Accelerator Alignment, ESRF, Grenoble, France, Oct. 3-7, (2016).
[55] P. V. C. Hough, US Patent 3 069 654 (1962).
[56] R. O. Duda and P. E. Hart, Comm. ACM **15**, 11 (1972).
[57] R. Frühwirth, Nucl. Instrum. Meth. A **262**, 444 (1987).
[58] Y. K. Semertzidis, J. Phys. Soc. Jpn. **85**, 091001 (2016).
[59] H. Yasuda, Development of High-precision detector alignment monitor for muon g-2/EDM measurements at J-PARC. *Master Thesis*, University of Tokyo (2018) [in Japanese].
[60] A. J. Silenko, Eur. Phys. J. C **77**, 695 (2017).